A Proposed Vertical Expansion Tunnel

N. J. Parziale[*] and J. Rabinovitch[*]

California Institute of Technology, Pasadena, California, 91125, USA

G. Blanquart[†], H. G. Hornung[‡] and J. E. Shepherd[§]

California Institute of Technology, Pasadena, California, 91125, USA

Issues resulting from the rupture of the secondary diaphragm in an expansion tunnel may be mitigated by matching the test gas pressure and the accelerator gas pressure, orienting the tunnel vertically, and initially separating the test gas from the accelerator gas by density stratification. Two benefits are: 1) the removal of the diaphragm particulates in the test gas after its rupture and 2) the elimination of the wave system that is a result of a real secondary diaphragm having a finite thickness and mass. An inviscid perfect-gas analysis is performed to find the reservoir conditions available in the vertical expansion tunnel (VET) for comparison to a conventional expansion tunnel (ET) and a reflected shock tunnel (RST). A numerical inviscid perfect-gas analysis is presented to estimate the available test time in the VET. The effective reservoir conditions of the VET lie somewhere between the RST and the ET.

Nomenclature

a	Local speed of sound, m/s
A	Jacobian matrix for a hyperbolic system of equations
α	Wave strength
$\mathcal{B}$	Wave strength multiplied by the corresponding eigenvector
D	Binary diffusion coefficient, m^2/s
$\mathbf{e}$	Eigenvector of the jacobian matrix
e	Total energy, J/m^3
E	Total energy multiplied by area, J/m
ET	Expansion tunnel
EW	Expansion wave
h	Mass specific enthalpy, MJ/kg
γ	Ratio of specific heats
L	Length, m
mw	Molecular weight
P	Pressure, Pa
PP	Particle path
ρ	Mass density, kg/m^3
$\mathcal{R}$	Mass density multiplied by cross-sectional area, kg/m
ϕ	Passive scalar used to track gas interfaces
Φ	Limiting function used for high-order corrctions
RST	Reflected shock tunnel
S	Cross-sectional area, m^2
SW	Shock wave
t	Time, s

[*]PhD Candidate, Graduate Aeronautical Laboratories, 1200 E. California Blvd. MC 205-45, AIAA Student Member.
[†]Assistant Professor, Mechanical Engineering, 1200 E. California Blvd. MC 104-44, AIAA Member.
[‡]Professor, Emeritus, Graduate Aeronautical Laboratories, 1200 E. California Blvd. MC 205-45, AIAA Fellow.
[§]Professor, Graduate Aeronautical Laboratories, 1200 E. California Blvd. MC 205-45, AIAA Member.

American Institute of Aeronautics and Astronautics

τ	Test Time, s
θ	Argument to be passed to limiting function
U	velocity in x direction, m/s
VET	Vertical Expansion Tunnel
$1D$	One-Dimensional
$2D$	Two-Dimensional
$3D$	Three-Dimensional

Subscript

A	Accelerator section
d	Diffusion
D	Driver section
i	State number
I	Intermediate section
N	Nozzle section
R	Reservoir conditions

I. Introduction

AN expansion tunnel is an impulse hypersonic facility used to simulate high-speed flows in a lab setting. As a result of the unsteady manner in which the test gas is processed, an expansion tunnel can reach a wider range of test conditions than a reflected shock tunnel, particularly in regard to effective reservoir enthalpy (h_R) and reservoir pressure (P_R). However, excessive amounts of noise in the test gas has proven to be problematic in the successful operation of an expansion tube or tunnel; reduction of this noise is critical.
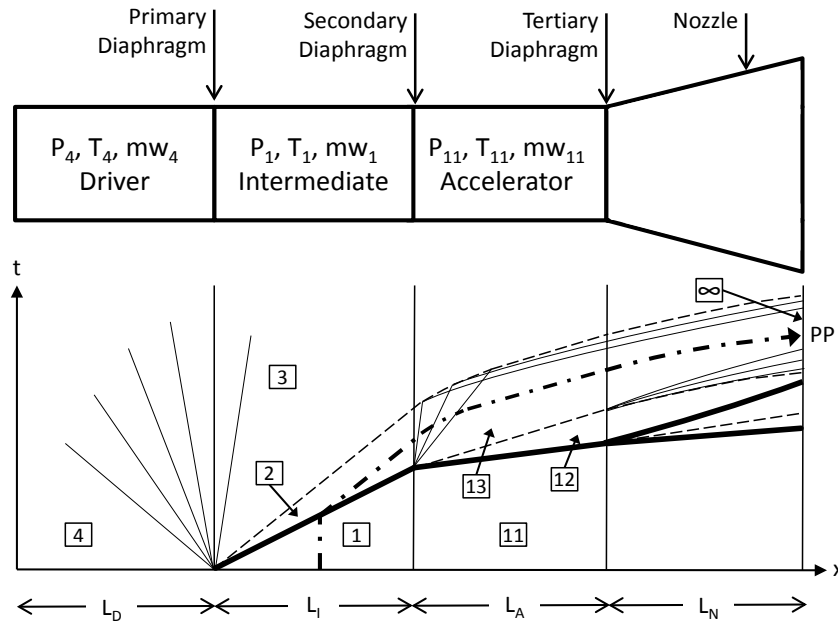

Figure 1. Above is a schematic of an expansion tunnel. The states $\boxed{4}$, $\boxed{1}$ and $\boxed{11}$ are the initial (or fill) conditions of the driver, the intermediate and the accelerator sections, respectively. Below is an x-t diagram sketch of expansion tunnel operation. Each numbered box represents a state in the expansion tunnel. Shock waves are shown as thick solid lines. Expansion characteristics are shown as thinner solid lines. The contact discontinuities are shown as dashed lines. A particle path (PP), representative of the test gas, is shown as a dashed-dot line. L_D, L_I, L_A and L_N are the lengths of the driver tube, the intermediate tube, the accelerator tube, and the nozzle, respectively.

The test gas in an expansion tunnel is processed in the following manner; first, the primary diaphragm is ruptured. As a result, a shock wave propagates into the intermediate tube, processing the test gas. Upon arrival of the shock wave at the secondary diaphragm station, the secondary diaphragm ruptures and a shock wave propagates into the accelerator tube. Concurrently, an unsteady expansion (centered at the secondary

diaphragm station) processes the test gas. The test gas is accelerated, first through this unsteady expansion, then (in the case of an expansion tunnel) through the diverging nozzle at the end of the accelerator tube. An expansion tunnel schematic and x-t diagram are presented in Figure 1.

Paul and Stalker[1] provide a thorough discussion of the issue of expansion tunnel noise. After the expansion tube and tunnel were proposed by Trimpi and Callis,[2,3] several facilities were constructed with mixed results.[4,5,6] Paul and Stalker[1] go on to show that acoustic waves generated in the driver gas, can, at certain conditions, be transmitted through the test gas/driver gas interface. This results in significant perturbations in the test gas. More recently, a number of expansion tube and expansion tunnel facilities have been constructed.[7,8,9,10,11,12] These facilities have been used successfully for hypersonic aerodynamics and supersonic combustion experiments. Still, many of the proceedings and articles show results from these facilities with significant test gas perturbations (often conveyed through Pitot pressure testing). In particular, many of these perturbations appear closest to the test gas/accelerator gas interface; this is evidence of the secondary diaphragm rupture adversely affecting the test gas.

To mitigate the effects of secondary diaphragm rupture in an expansion tunnel, the secondary diaphragm can be eliminated in the following manner: orient the facility vertically and separate the intermediate and accelerator tubes (filled to the same initial pressure, with gases of different density, light over heavy) by a fast acting sliding valve. The fast acting sliding valve will be removed prior to the bursting of the primary diaphragm, leaving a hydrodynamically stable intermediate/accelerator gas interface; the benefits of which are a lack of diaphragm particulate in the test gas and the elimination of the wave system that is a result of a real secondary diaphragm having a finite thickness and mass.

In this paper a vertical expansion tunnel (VET) is proposed. The advantages and disadvantages of this type of hypersonic ground-test facility are discussed. A detailed analysis of a VET with a cold driver is performed, including a perfect-gas calculation of available parameter space accompanied by perfect-gas quasi-1D gas dynamic computations to estimate the test time. A comparison of the VET to other types of hypersonic facilities is made. It is found that the achievable effective reservoir enthalpy of the VET lies somewhere between the reflected shock tunnel and the conventional expansion tunnel.

II.   Initial Estimate of Available Conditions

In this section, an estimate of the available test conditions from a VET for perfect-gas conditions with a cold driver is made. The effective reservoir conditions achievable in the VET are compared to those in a conventional expansion tunnel (ET) and reflected shock tunnel (RST). The driver pressure (P_4) is limited so that it can be filled by conventional gas bottles. The pressure in the intermediate tube (P_1) is chosen so that the test gas reaches a maximum temperature of $\approx$2000 K, so the perfect-gas assumption holds. Pressure-velocity diagrams are used (Figure 2) to compute the conditions of the test gas as it is processed by the non-steady wave systems (for reference, follow the particle path, PP, in Figure 1). The static pressure and velocity must be matched in states $\boxed{2}$ and $\boxed{3}$ and in states $\boxed{12}$ and $\boxed{13}$. This is done by plotting

$$\frac{P_3}{P_4} = \left(1 - \frac{(\gamma_4 - 1)(U_3 - U_4)}{2a_4}\right)^{\frac{2\gamma_4}{\gamma_4 - 1}}, \tag{1}$$

and

$$\frac{U_2 - U_1}{a_1} = \frac{P_2 - P_1}{\gamma_1 P_1 \sqrt{1 + \frac{(\gamma_1 + 1)(P_2 - P_1)}{2\gamma_1 P_1}}}, \tag{2}$$

in pressure - velocity space and finding the point of intersection.[13] Here, γ is the ratio of specific heats, P is the static pressure, U is the velocity, and a is the sound speed. Equations 1 and 2 are annotated for finding the conditions after primary diaphragm rupture and are analogous to the equations that would be used to evaluate the states $\boxed{12}$ and $\boxed{13}$.

Two pressure-velocity diagrams are presented in Figure 2. On the left is an expansion tunnel in a conventional arrangement, with a diaphragm located between the intermediate and accelerator chambers. This setup allows for a mismatch of the pressures in the intermediate and accelerator chambers, and thus a higher available flow speed at the nozzle exit due to a more efficient expansion of the test gas. If some sacrifice of the reservoir conditions can be made, the secondary diaphragm may be eliminated by matching the pressure in the intermediate and accelerator tubes, separating them by density stratification, and orienting the facility vertically (Figure 2(b)).

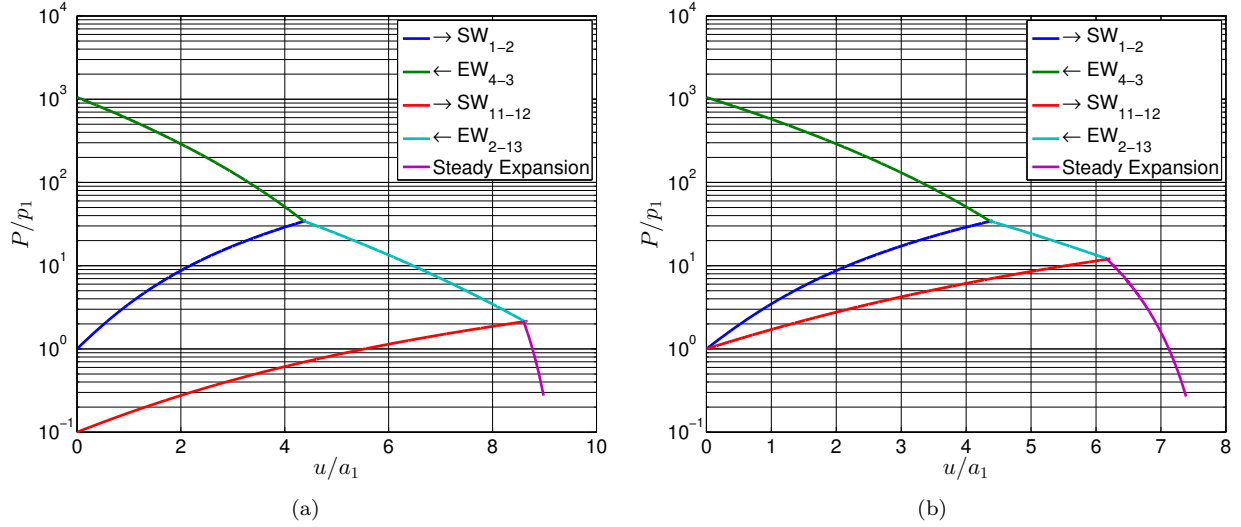American Institute of Aeronautics and Astronautics

Figure 2. Pressure - velocity diagrams for the conventional (left (a)) and vertical expansion tunnel (right (b)) for the same driver gas/test gas fill pressure ratio. In each plot are lines marking shock waves (SW_{A-B}), expansion waves (EW_{A-B}), and the steady expansion. The primary differences are matched pressures in states $\boxed{1}$ and $\boxed{11}$ and a lower velocity as the end of the steady expansion for a given driver gas/test gas fill pressure ratio in the vertical expansion tunnel as opposed to the conventional expansion tunnel.

Table 1. Comparison of run conditions available for a conventional expansion tunnel (ET) and a vertical expansion tunnel (VET) for set of given fill pressures. Also, listed are the conditions for a reflected shock tunnel (RST) when operated at a taylored condition (RST-1). Taylored shock tunnel operation ensures the longest possible test time. RST-2 is a condition where the reservoir temperature is permitted to reach 2000K, the maximum temperature reached in the ET and VET cases. P_4, P_1 and P_{11} are the initial pressures of the driver, intermediate, and accelerator sections, respectively. h_R and P_R are the effective reservoir enthalpy and pressure. T_{Max} is the maximum temperature the test gas is raised to in the facility. U_∞, P_∞, ρ_∞, T_∞, and M_∞ are the free-stream velocity, pressure, density, temperature, and Mach number, respectively. For comparison purposes, the flows are all expanded to Mach 6 at the nozzle exit.

	P_4 [He] (MPa)	P_1 [Air] (kPa)	P_{11}[He] (kPa)	h_R (MJ/kg)	P_R (MPa)	T_{Max} (K)	U_∞ (km/s)	P_∞ (kPa)	ρ_∞ (kg/m^3)	T_∞ (K)	M_∞ (–)
ET	8.16	7.75	0.35	6.0	12	2000	3.3	7.9	0.037	733	6.0
VET	8.16	7.75	7.75	3.8	2.4	2000	2.6	1.5	0.012	459	6.0
RST-1	8.16	106	NA	1.8	7.8	1780	1.8	4.9	0.079	217	6.0
RST-2	8.16	75.0	NA	2.0	6.7	2030	1.9	4.2	0.060	247	6.0
RST-3	8.16	7.10	NA	3.8	1.9	3200	2.6	0.6	0.004	490	6.0

The available conditions for a given set of fill pressures are tabulated (Table 1) for three types of impulse hypersonic facilities, the VET, the ET, and the RST. Again, the driver pressure (P_4) is limited to 1200 psi, so that it can be filled by conventional gas bottles. The pressure in the intermediate tube of the ET and VET is chosen such that the temperature in the gas does not exceed 2000 K. The pressure in the accelerator tube in the ET is chosen by an estimate of the practical restraints (this will be explained in more detail in the following section). The effective reservoir conditions for the ET and the VET are found by isentropic compression to rest after the non-steady expansion from state $\boxed{13}$. The free-stream conditions for all facilities are expanded to a Mach number of six for comparison. The pressure, P_1, for the first shock tunnel case (RST-1) is chosen such that it is operated in the taylored mode. The pressure, P_1, for the second shock tunnel case (RST-2) is chosen such that the temperature in the test gas does not exceed 2000 K. The 2000 K limit is imposed to maintain the perfect-gas assumption and required a 10% increase in the Mach number of the primary shock relative to the taylored condition (as in RST-1). The pressure, P_1, for the third shock tunnel case (RST-3) is chosen such that the reservoir enthalpy is matched to the VET case and required a 50% increase in the Mach number of the primary shock relative to the taylored condition (as in RST-1). In this case, the test gas will be reacting, so Cantera[14] with the Shock and Detonation Toolbox[15] is used to evaluate the conditions in the reservoir and through the nozzle. The thermodynamic data[16,17] and reaction

American Institute of Aeronautics and Astronautics

rates[18] are found in the literature. The test gas is assumed to be in chemical equilibrium from the reservoir to the throat of the nozzle, and is then in chemical non-equilibrium[19] from the throat to the end of the 10° half angle nozzle.

If the quantity of interest in ground-test facilities is effective reservoir conditions, then the capability of the VET lies between the ET and the RST. Herein lies one of the advantages of the expansion tunnel over the shock tunnel: the maximum temperature of the test gas is lower for a given run condition. The detrimental effects of the test gas being partially dissociated and partially vibrationally excited are less severe in a ET than a RST; for example, in the RST-3 case there is 3.8% NO in the free-stream.

III.   Practical Considerations for a VET

Significant perturbations in the mean flow of the test gas can result from acoustic waves being transmitted through the contact discontinuity between states $\boxed{2}$ and $\boxed{3}$.[1] Previous experiments conducted in the expansion tube at the University of Illinois at Urbana Champaign[12] have suggested that the upper limit for the speed of sound ratio between the contact discontinuity is around $c_3/c_2 \approx 0.5$ to avoid an acoustic "focusing" effect. This criterion will be followed when specifying the tube fill pressures.

The intermediate and accelerator chambers are to be separated by a fast acting sliding valve. This sliding valve will separate the two tubes during filling, and then be pulled away right before the primary diaphragm is burst. The helium in the accelerator tube will diffuse into the intermediate tube after the sliding valve is pulled away. A characteristic diffusion length scale, L_d, associated with helium and air can be approximated as $L_d = \sqrt{Dt_d}$, where D is the binary diffusion coefficient for air and helium, and t_d is a characteristic time. For practical tube fill pressures ($p_1, p_{11} \approx 10$ kPa), $D \approx 0.001$ m^2/s,[20] which translates to a diffusion distance of about $L_d = 3$ mm in $t_d = 10$ ms. This should prove to be an acceptable diffusion length and opening time.

Maximizing the test time is of paramount importance in such an impulse hypersonic facility. Trimpi and Callis[2,3] make some assumptions about how the wave systems form in the expansion tunnel to intelligently select the length of each section. Furthermore, the starting time of the nozzle[3,21] and the wall boundary layer[22] must be considered when sizing a proposed facility. Procedures for finding estimates of the test time in an expansion tube can be found in the literature;[1,12] but, in order to include the nozzle geometry, non-steady Euler simulations are necessary to find more accurate estimates of the test time.

IV.   Expansion Tunnel Sizing

In this section the basic methodology is explained that was used to decide upon the dimensions used in the numerical simulations for a VET. All of the following calculations assume that the inner diameter of the driver section, intermediate section, and accelerator section is only 0.0254 m. This is a relatively small diameter, which makes the entire facility under 4 m long, or under two-stories tall. Since the test time scales linearly with diameter, it is very easy to see how this design could be applied to larger facilities.

Due to viscous effects, boundary layers will begin to form along the tube walls in the facility, which will cause the shockwave produced to decelerate. In order to mitigate the viscous effects on the facility, care must be taken when choosing the ratio L/d, where L is the sum of the lengths of the intermediate and accelerator sections, and d is the diameter of the tube used for the intermediate and accelerator sections. The higher this ratio is, the more significant the viscous effects will be. Based on previous studies, a very conservative value of $L/d = 50$ is chosen for this study ($L = 1.27$ m), which will ensure that viscous effects are negligible in this facility.[23] As the test time scales linearly with L, the test times predicted from this analysis are therefore very conservative in nature.

Once the diameter of the tube for the intermediate and accelerator sections is chosen, and the maximum length of the intermediate and accelerator sections is prescribed, it is necessary to have an idea of what fill pressures are desired in order to scale the lengths of the intermediate and accelerator tubes appropriately. The maximum fill pressure for the driver section of 8.16 MPa (just under 1200 PSI) is chosen so that it may be filled from conventional helium bottles. Helium will also be used in the driver section due to its relatively high sound speed. Once this pressure is chosen, the parameters chosen for the intermediate tube (air) and accelerator tube (helium) will determine the test conditions. However, these conditions must be chosen in such a way that the ratio of c_3/c_2 is not much greater than 0.5, as previously discussed. Decreasing the value of c_3/c_2 can be achieved simply by increasing the pressure ratio P_4/P_1. For these reasons, a fill

American Institute of Aeronautics and Astronautics

pressure of 7.75 kPa is chosen for the intermediate and accelerator sections. This gives a pressure ratio of approximately 1050, which corresponds to a c_3/c_2 ratio of approximately 0.57, which should be acceptable for noise considerations. This also keeps the maximum static temperature reached in the facility below 2000 K, as previously discussed.

Once the ideal fill pressures have been chosen, the optimal lengths for the different sections must be chosen, keeping in mind the previously prescribed constraint that L/d must not exceed 50. In order to calculate both the theoretical test time in an expansion tube with no nozzle, and to pick the optimal lengths for the different sections, an x-t diagram focused on the test time is useful. In Figure 3 the ideal test time is labeled, and it corresponds to the time between the contact discontinuity created by the transmitted shock, and intersection of the tail and the reflected head of the secondary expansion wave. The head of the expansion wave reflects off of the initial contact discontinuity generated when the primary diaphragm ruptures. Although the reflected head of the expansion wave is plotted as a straight line, it is in fact curved in the non-simple wave region bounded by the tail of the expansion wave and the initial contact discontinuity. In addition, the original contact discontinuity begins to curve downwards in x-t space after the first wave from the expansion wave intersects with it. It is possible to calculate the analytical intersection between the reflected head of the expansion wave and the tail of the expansion, and this gives the location of the optimal test time.[12, 24] However, in the 1D case, if the test section is not located at the ideal location, the test time will be limited either by the head of the expansion wave, or by the reflected tail of the expansion wave. With L/d limited to 50, the ideal lengths for the intermediate and accelerator tubes are 0.86 m and 0.41 m respectively.
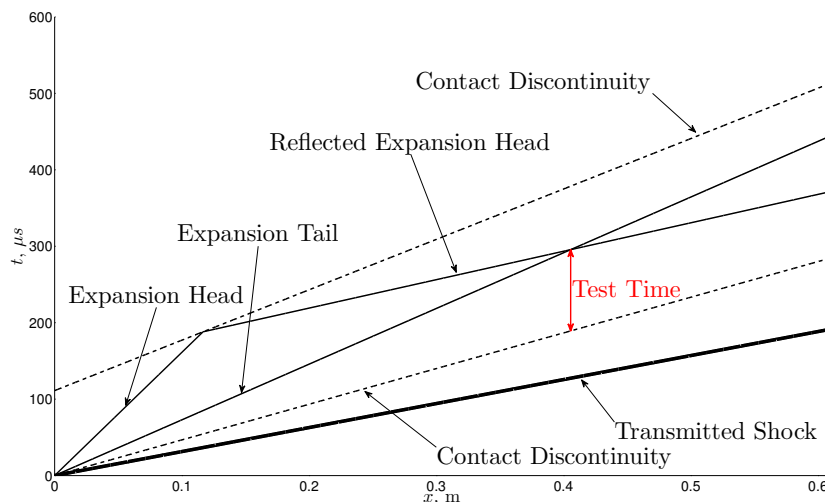

Figure 3. Schematic x-t diagram focusing on the accelerator tube, and the ideal test time for an expansion tube with no nozzle. All times and lengths are physical and based on calculations performed using the method of characteristics with previously stated fill pressures. Note that while the reflected head of the expansion wave is plotted as a straight line, it is actually curved in the non-simple wave region bounded by the tail of the expansion wave and the original contact discontinuity. In addition, the original contact discontinuity also begins to curve after the first wave from the expansion head intersects with it. $t = 0$ μs corresponds to when the shock reaches the interface of the intermediate and accelerator section, and $x = 0$ m corresponds to the start of the accelerator tube.

The addition of a nozzle at the end of the accelerator section makes the length selection process for the intermediate and accelerator tubes more complicated. The test time is still limited by the arrival of the reflected expansion head, but now the location of the nozzle has a large effect on the test time. In order to allow the test gas to expand through the nozzle before the reflected expansion head wave arrives, it was found that putting the nozzle upstream of the ideal accelerator tube length gave the best results. Numerical simulations are used in order to help better understand the effect that expanding the flow will have on the test time of the system, and this will be discussed in more detail in the next section.

American Institute of Aeronautics and Astronautics

V.   Numerical Methods

While it is possible to solve the 1D problem analytically as shown previously, as soon as a nozzle is added, the problem becomes inherently 2D or 3D. The problem can still be cast in a 1D configuration, but analytical solutions no longer exist to describe the test time after the nozzle has expanded the flow. In this case, numerical simulations are very useful when trying to estimate the duration of the test time. The present analysis is performed assuming that all the gases behave as ideal gases, and that no chemical reactions occur throughout the experiment. Due to the relatively low static temperatures reached by the gases throughout the different states, this is a valid assumption. In addition, it is assumed that there is no mixing between any of the gases at the fluid interfaces as a result of the short run time.

V.A.   The Compressible Euler Equations with an Area Change

In order to explore a large parameter space at a relatively low computational cost, quasi 1D simulations are performed based on a method suggested by Glaister.[25] A brief summary of this method is presented below.

In three dimensions, and in a general orthogonal coordinate system given by (x_1, x_2, x_3), the Euler equations are given by Eq. 3-5.

$$\rho_t + \nabla \cdot (\rho \mathbf{u}) = 0 \tag{3}$$

$$(\rho \mathbf{u})_t + \nabla \cdot (\rho \mathbf{u}\mathbf{u}) = -\nabla p \tag{4}$$

$$e_t + \nabla \cdot [\mathbf{u}(e + p)] = 0 \tag{5}$$

Combining these with Eq. 6, the equation of state for an ideal gas, allows the flow of an unsteady compressible inviscid fluid to be solved for.

$$e = \frac{p}{\gamma - 1} + \frac{1}{2}\rho \mathbf{u} \cdot \mathbf{u} \tag{6}$$

Here, $\rho = \rho(\mathbf{x}, t)$, $p = p(\mathbf{x}, t)$, $e = e(\mathbf{x}, t)$, and $\mathbf{u} = \mathbf{u}(\mathbf{x}, t) = [u_1(\mathbf{x}, t), u_2(\mathbf{x}, t), [u_3(\mathbf{x}, t)]^{\mathrm{T}}$ represent the density, pressure, total energy, and the three components of velocity, respectively, at a general position in space given by $\mathbf{x} = (x_1, x_2, x_3)^{\mathrm{T}}$ and at time t. The divergence and gradient operators are left in a general form, and to evaluate these equations, the appropriate operator must be used based on the chosen coordinate system.

In a general 3D orthogonal coordinate system, a line element $d\mathbf{s}$ can be written as

$$d\mathbf{s} = \xi_1 dx_1 \hat{\mathbf{x}}_\mathbf{1} + \xi_2 dx_2 \hat{\mathbf{x}}_\mathbf{2} + \xi_3 dx_3 \hat{\mathbf{x}}_\mathbf{3}. \tag{7}$$

In Eq. 7, $\hat{\mathbf{x}}_\mathbf{1}$, $\hat{\mathbf{x}}_\mathbf{2}$, and $\hat{\mathbf{x}}_\mathbf{3}$ are the unit vectors parallel to their specific coordinate lines. Assuming an ideal nozzle, all changes in the flow depend only on one coordinate direction. In this case, it is assumed that all variables are a function of only x_1 and t, where the x_1 coordinate corresponds to the location along the centerline of the nozzle. It is now possible to write $\mathbf{u} = [u(x_1, t), 0, 0]^{\mathrm{T}} = u$, which is a parallel flow assumption, and is only valid for nozzles where the nozzle area varies relatively slowly. With this simplifying assumption, Eq. 3 - 5 can be rewritten as follows

$$(\xi_1 \xi_2 \xi_3 \rho)_t + (\xi_2 \xi_3 \rho u)_{x_1} = 0 \tag{8}$$

$$(\xi_1 \xi_2 \xi_3 \rho u)_t + (\xi_2 \xi_3 \rho u^2)_{x_1} = -\xi_2 \xi_3 \frac{\partial p}{\partial x_1} \tag{9}$$

$$(\xi_1 \xi_2 \xi_3 e)_t + [\xi_2 \xi_3 u(e + p)]_{x_1} = 0 \tag{10}$$

In order to describe compressible fluid flow through a duct of smoothly varying cross section, ξ_1 can be an arbitrary constant, and here it is assumed that $\xi_1 = 1$. Using this assumption, it is now possible to once again rewrite the Euler equations as

$$(\xi_2 \xi_3 \rho)_t + (\xi_2 \xi_3 \rho u)_{x_1} = 0 \tag{11}$$

$$(\xi_2 \xi_3 \rho u)_t + [\xi_2 \xi_3 (p + \rho u^2)]_{x_1} = p\frac{\partial}{\partial x_1}(\xi_2 \xi_3) \tag{12}$$

$$(\xi_2 \xi_3 e)_t + [\xi_2 \xi_3 u(e + p)]_{x_1} = 0 \tag{13}$$

American Institute of Aeronautics and Astronautics

In the above equations, the left hand side is similar to the 1D compressible Euler equations in conservative form, while there is an additional source term added to the right hand side that is not present in the classic 1D Euler equations. In order to simplify these equations further, Glaister uses the notation $S(r) = \xi_1\xi_2$, so that $S(r)$ represents the cross-sectional area of the duct at a point r, where r is the distance in the x_1 direction. This system of equations can then be written as

$$[S(r)\mathbf{w}]_t + [S(r)\mathbf{f}(\mathbf{w})]_r = \mathbf{g}(\mathbf{w}), \tag{14}$$

where

$$\mathbf{w} = \begin{pmatrix} \rho \\ \rho u \\ e \end{pmatrix}, \quad \mathbf{f}(\mathbf{w}) = \begin{pmatrix} \rho u \\ p + \rho u^2 \\ u(e + p) \end{pmatrix} \quad \text{and} \quad \mathbf{g}(\mathbf{w}) = \begin{pmatrix} 0 \\ pS'(r) \\ 0 \end{pmatrix}. \tag{15}$$

Note that it is also possible to attain Eq. 15 by integrating the Euler equations over a cross section at a given point in space. It can be shown that $S(r)\mathbf{f}(\mathbf{w}) = \mathbf{f}[S(r)\mathbf{w}]$ which will be called $\mathbf{F}(\mathbf{W})$, and that $S(r)\mathbf{w}_t = [S(r)\mathbf{w}]_t$, assuming that the geometry of the domain does not change with time. This allows Eq. 14 to be re-written as,

$$\mathbf{W}_t + [\mathbf{F}(\mathbf{W})]_r = \mathbf{g}(\mathbf{w}), \tag{16}$$

where $\mathbf{W} = S(r)\mathbf{w}$. Following the terminology used by Glaister, this gives rise to a new set of 'conserved' variables; $\mathcal{R}$, E, and $\mathcal{P}$. $\mathcal{R} = S(r)\rho$, $E = S(r)e$ and $\mathcal{P} = S(r)p$. It is important to note that with these new conserved variables, the gas velocity, speed of sound, and enthalpy remain the same: $U = u$, $a = \sqrt{\gamma p/\rho} = \sqrt{\gamma\mathcal{P}/\mathcal{R}}$, and $h = (e+p)/\rho = (E+\mathcal{P})/\mathcal{R} = H$. In addition, the Jacobian remains unchanged:

$$\mathbf{A} = \frac{\partial \mathbf{F}(\mathbf{W})}{\partial \mathbf{W}} = \frac{\partial \mathbf{f}(\mathbf{w})}{\partial \mathbf{w}}. \tag{17}$$

Finally, the Euler equations for duct flow are written as

$$\begin{pmatrix} \mathcal{R} \\ \mathcal{R}U \\ E \end{pmatrix}_t + \begin{pmatrix} \mathcal{R}U \\ \mathcal{P} + \mathcal{R}U^2 \\ U(E + \mathcal{P}) \end{pmatrix} = \begin{pmatrix} 0 \\ \mathcal{P}\frac{S'(r)}{S(r)} \\ 0 \end{pmatrix}. \tag{18}$$

with

$$E = \frac{\mathcal{P}}{\gamma - 1} + \frac{1}{2}\mathcal{R}U^2. \tag{19}$$

V.B. Roe Solver

A standard Roe Riemann Solver[26] will be used to solve these equations. To denote Roe averaged values, the notation $\tilde{Y}$ will be used, where

$$\tilde{Y} = \frac{\sqrt{\mathcal{R}_L}Y_L + \sqrt{\mathcal{R}_R}Y_R}{\sqrt{\mathcal{R}_R} + \sqrt{\mathcal{R}_L}}. \tag{20}$$

L and R refer to the left and right cell values, as the averaged quanties are calculated at cell interfaces. The eigenvalues of $\tilde{\mathbf{A}}$ can be calculated to be

$$\tilde{\lambda}^{(1)} = \tilde{U} - \tilde{a}, \quad \tilde{\lambda}^{(2)} = \tilde{U}, \quad \tilde{\lambda}^{(3)} = \tilde{U} + \tilde{a} \tag{21}$$

with corresponding eigenvectors of

$$\tilde{\mathbf{e}}^{(1)} = \begin{pmatrix} 1 \\ \tilde{U} - \tilde{a} \\ \tilde{H} - \tilde{U}\tilde{a} \end{pmatrix}, \quad \tilde{\mathbf{e}}^{(2)} = \begin{pmatrix} 1 \\ \tilde{U} \\ \frac{1}{2}\tilde{U}^2 \end{pmatrix} \quad \text{and} \quad \tilde{\mathbf{e}}^{(3)} = \begin{pmatrix} 1 \\ \tilde{U} + \tilde{a} \\ \tilde{H} + \tilde{U}\tilde{a} \end{pmatrix}, \tag{22}$$

where $\tilde{a} = (\gamma - 1)(\tilde{H} - \frac{1}{2}\tilde{U}^2)$.

American Institute of Aeronautics and Astronautics

A numerical approximation for $\tilde{\mathbf{g}}(\mathbf{w})$ must be used, and Glaister proposed that

$$\tilde{g}_2(\mathbf{w}^n) = \frac{S_j - S_{j-1}}{\Delta r} \frac{\tilde{\rho}\tilde{a}^2}{\gamma} \tag{23}$$

is a natural choice for this approximation. Here, S_j represents the average cross sectional area over cell j. With this notation, it is easy to see that to go from this new set of conserved variables to the more traditional set of conserved variables, the simple relation of $\mathbf{w}_j^n = \frac{\mathbf{W}_j^n}{\hat{S}_j}$ must be used.

The fluxes are projected onto the eigenvectors of the system so that a standard explicit update step can be employed. In addition to the standard wave strengths being obtained for the Euler equations, $\tilde{\mathbf{g}}(\mathbf{w}^n)$ is also projected onto the eigenvectors which modifies the standard wave strengths that result from the Euler equations. Cell values are updated using a flux difference splitting method which is outlined in Eq. 24.

$$\mathbf{W}_j^{n+1} = \mathbf{W}_j^n - \frac{\Delta t}{\Delta r} \left(\sum_{\tilde{\lambda}_{j+\frac{1}{2}}^{(i)} \leq 0} \tilde{\lambda}_{j+\frac{1}{2}}^{(i)} \tilde{\gamma}_{j+\frac{1}{2}}^{(i)} \tilde{\mathbf{e}}_{j+\frac{1}{2}}^{(i)} + \sum_{\tilde{\lambda}_{j-\frac{1}{2}}^{(i)} \geq 0} \tilde{\lambda}_{j-\frac{1}{2}}^{(i)} \tilde{\gamma}_{j-\frac{1}{2}}^{(i)} \tilde{\mathbf{e}}_{j-\frac{1}{2}}^{(i)} \right) \tag{24}$$

Here, the summations are performed over i, where $i = 1, 2, 3$. The subscripts refer to the cell interface $(j \pm 1/2)$ where each value is calculated, the regular superscripts (n) correspond to a time step, and the superscripts in brackets (i) correspond to a component $(i = 1, 2, 3)$.

Here, $\tilde{\gamma}^{(i)}$ refers to the modified wave strength, where

$$\tilde{\gamma}^{(i)} = \tilde{\alpha}^{(i)} + \tilde{\beta}^{(i)}/\tilde{\lambda}^{(i)}. \tag{25}$$

The $\tilde{\alpha}^{(i)}$ wave strengths are the standard Roe-averaged wave strengths, where

$$\tilde{\alpha}^{(1)} = \frac{1}{2\tilde{a}^2}(\Delta_r \mathcal{P} - \tilde{\mathcal{R}}\tilde{a}\Delta_r U), \quad \tilde{\alpha}^{(2)} = \Delta_r \mathcal{R} - \frac{\Delta_r \mathcal{P}}{\tilde{a}^2} \quad \text{and} \quad \tilde{\alpha}^{(3)} = \frac{1}{2\tilde{a}^2}(\Delta_r \mathcal{P} + \tilde{\mathcal{R}}\tilde{a}\Delta_r U). \tag{26}$$

The Δ_r operator is the difference in value between different cells, so that $\Delta_r U_{j+1/2} = U_{j+1} - U_j$. The $\tilde{\beta}^{(i)}$ in Eq. 24 takes into account changes in cross sectional area and can be expressed as

$$\tilde{\beta}^{(1)} = \frac{\tilde{\mathcal{R}}\Delta_r S}{2\gamma \tilde{S}}[(\gamma - 1)\tilde{U} + \tilde{a}], \quad \tilde{\beta}^{(2)} = -\frac{(\gamma - 1)\tilde{\mathcal{R}}\tilde{U}\Delta_r S}{\gamma \tilde{S}}, \quad \text{and} \quad \tilde{\beta}^{(3)} = \frac{\tilde{\mathcal{R}}\Delta_r S}{2\gamma \tilde{S}}[(\gamma - 1)\tilde{U} - \tilde{a}], \tag{27}$$

where $\tilde{S}_{j+1/2} = \sqrt{S_{j+1}S_j}$.

V.C. Treatment of Fluid Interfaces

The above numerical method assumes that γ is constant for every cell in the domain. This is not true for the present investigation. It is very easy to create unphysical oscillations at the interface between two different fluids if no special care is taken when calculating values at the fluid interfaces. A modification to the above scheme is used that was originally suggested by Abgrall and Karni.[27]

Abgrall and Karni suggested that a simple way to avoid unphysical oscillations at fluid interfaces is to calculate two separate fluxes between the different fluids. A schematic explaining this method is shown in Figure 4, where the cell face at $j + \frac{1}{2}$ is the interface between two different fluids with two different ratios of specific heats, γ_1 and γ_2 respectively. When updating cell j, γ_1 is used to calculate the properties needed at $j + \frac{1}{2}$, and when updating cell $j + 1$, γ_2 is used to calculate the values needed at $j + \frac{1}{2}$. In addition, the timing as to when the γ values are updated in the domain based on a scalar transport equation has to be performed carefully. A more detailed explanation can be found in Abgrall and Karni's original paper.[27]

The drawback is that this scheme no longer conserves total energy since two different fluxes are calculated at the same interface. In addition, the scheme uses "frozen" thermodynamics, or γ values from the previous time step to calculate the new values. Abgrall and Karni show that across a material interface where pressure and velocity are constant (a standard contact discontinuity), the errors induced due to the different fluxes used and the lag in updating γ are actually opposite in sign, and very similar in magnitude. In addition, there are only three material interfaces in the current simulations, and these interfaces are the only places where total energy is not conserved. When the number of grid points in the domain is increased, the relative

American Institute of Aeronautics and Astronautics

loss of total energy reduces. It has been checked that the loss of total energy in the simulations run for this investigation are negligible.
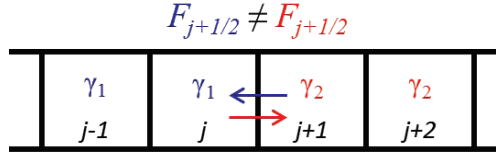

$$F_{j+1/2} \neq F_{j+1/2}$$

Figure 4. Schematic for the flux correction suggested by Abgrall and Karni when dealing with an interface between two different fluids.

V.D. Level Set

In order to accurately describe the location of the different fluids, a method has to be implemented to track the location of the fluid interfaces. A simple advection equation (Eq. 28) is solved where ϕ is a passive scalar.

$$\frac{\partial \phi}{\partial t} + u \frac{\partial \phi}{\partial x} = 0 \tag{28}$$

The levelset function, ϕ, is used to determine the location of the different gases. For the case where the driver and accelerator gases are the same and the test gas is different, it is simple to assign ϕ an initial value of 1 in the driver and accelerator sections, and a value of -1 in the intermediate section. If a nozzle is used, it is assumed that the nozzle will be filled with low pressure air, and therefore ϕ is this section is also assigned a value of -1. After advecting ϕ, a hard switch is employed such that if $\phi \geq 0$, the properties of driver/accelerator gas are used; and if $\phi < 0$, the properties of the intermediate gas are used.

A modified semi-lagrangian scalar scheme[28] is used to solve Eq. 28.

V.E. Higher-Order Corrections

The numerical scheme explained in Section V.B is first order at best and very diffusive, which means shocks and contact discontinuities are unphysically spread over many grid cells. To help alleviate this problem, a high-order flux correction is added using wave limiters.[29] In order to implement this, an additional term is added to Eq. 24, so that it now becomes

$$\mathbf{W}_j^{n+1} = \mathbf{W}_j^n - \frac{\Delta t}{\Delta r} \left(\sum_{\tilde{\lambda}_{j+\frac{1}{2}}^{(i)} \leq 0} \tilde{\lambda}_{j+\frac{1}{2}}^{(i)} \tilde{\gamma}_{j+\frac{1}{2}}^{(i)} \tilde{\mathbf{e}}_{j+\frac{1}{2}}^{(i)} + \sum_{\tilde{\lambda}_{j-\frac{1}{2}}^{(i)} \geq 0} \tilde{\lambda}_{j-\frac{1}{2}}^{(i)} \tilde{\gamma}_{j-\frac{1}{2}}^{(i)} \tilde{\mathbf{e}}_{j-\frac{1}{2}}^{(i)} \right) - \frac{\Delta t}{\Delta r} (\hat{\mathbf{F}}_{j+\frac{1}{2}} - \hat{\mathbf{F}}_{j-\frac{1}{2}}) \tag{29}$$

where

$$\hat{\mathbf{F}}_{j-\frac{1}{2}} = \frac{1}{2} \sum_{i=1}^{3} |\tilde{\lambda}_{j-\frac{1}{2}}^{(i)}| \left(1 - \frac{\Delta t}{\Delta r} |\tilde{\lambda}_{j-\frac{1}{2}}^{(i)}| \right) \tilde{\mathcal{B}}_{j-\frac{1}{2}}^{(i)}. \tag{30}$$

$\tilde{\mathcal{B}}_{j-\frac{1}{2}}^{(i)} = \Phi(\theta_{j-\frac{1}{2}}^{(i)}) \mathcal{B}_{j-\frac{1}{2}}^{(i)}$, where $\Phi(\theta)$ is a limiting function, and $\mathcal{B}_{j-\frac{1}{2}}^{(i)} = \tilde{\alpha}_{j-\frac{1}{2}}^{(i)} \tilde{\mathbf{e}}_{j-\frac{1}{2}}^{(i)}$. A Van Leer limiting function is used:[30]

$$\Phi(\theta) = \frac{\theta + |\theta|}{1 + \theta}. \tag{31}$$

A careful choice must be made for θ in order to deal with the relatively large change in properties at the interfaces between the different sections of the Expansion Tunnel. The initial pressure ratio of ≈ 1000 between the driver gas and intermediate gas creates extremely steep gradients and rapidly changing eigenvectors. Lax and Liu[31] suggested a robust function for θ that is designed to work with systems of non-linear equations. They define

$$\theta_{j-\frac{1}{2}}^{(i)} = \frac{\hat{\mathcal{B}}_{J-\frac{1}{2}}^{(i)} \cdot \mathcal{B}_{j-\frac{1}{2}}^{(i)}}{\mathcal{B}_{j-\frac{1}{2}}^{(i)} \cdot \mathcal{B}_{j-\frac{1}{2}}^{(i)}} \tag{32}$$

American Institute of Aeronautics and Astronautics

where

$$\hat{\mathcal{B}}_{J-\frac{1}{2}}^{(i)} = (\tilde{\mathbf{l}}_{j-\frac{1}{2}}^{(i)} \Delta \mathbf{W}_{J-\frac{1}{2}}) \tilde{\mathbf{e}}_{j-\frac{1}{2}}^{(i)} \tag{33}$$

and $\tilde{\mathbf{l}}$ is the appropriate left eigenvector using Roe-averaged quantities. In addition, J changes value based on the sign of the eigenvector, so that the limiting is performed in an upwinded or downwinded manner as necessary, so

$$J = \begin{cases} j - 1 & \text{if } \tilde{\lambda}_{j-\frac{1}{2}}^{(i)} > 0 \\ j + 1 & \text{if } \tilde{\lambda}_{j-\frac{1}{2}}^{(i)} < 0 \end{cases} \tag{34}$$

These higher-order corrections do a good job at making both contact discontinuities and shocks much sharper in the simulations. The flux limiters are not used in the vicinity of walls, or right at the interface between two fluids with different values of γ.

V.F.   Entropy Fix

Due to the large pressure ratios needed initially in order to achieve relevant test conditions, an entropy fix is required to avoid entropy-violating (expansion) shocks in the solution. The entropy fix proposed by Sanders et al.[32] is implemented, and no entropy violating solutions are observed.

VI.   Numerical Results

In this section, the numerical results obtained are presented. In order to validate the numerical methods used, comparisons were made between analytic values calculated and 1D numerical simulations. After good agreement was achieved in 1D, simulations were run in quasi-1D (non-uniform cross-sectional area) to simulate adding a conical nozzle to the end of the accelerator section.

VI.A.   1D Results

A 1D numerical simulation with the same initial conditions as Figure 2(b) was performed in order to validate the numerical method used. As the simulation did not include the nozzle, the "Steady Expansion" section is not included, which corresponds to the flow passing through a diverging nozzle. In this simulation, $L_D = 2.0$ m, $L_I = 0.86$ m, and $L_A = 1.0$ m. The subscripts correspond to the driver section, intermediate section, and accelerator section respectively. The accelerator section is made longer in order to check that the wave pattern predicted in Figure 3 matches the wave pattern produced in the simulations. The primary diaphragm is located at $x = 0$ m, and the interface between the intermediate and accelerator sections is at $x = 0.86$ m. The gas properties are: $\rho_D = 13.1$ kg/m³, $P_D = 8.16$ MPa, $\rho_I = 0.0901$ kg/m³, $P_I = 7.75$ kPa, $\rho_A = 0.0124$ kg/m³, and $P_A = 7.75$ kPa. Helium is used both in the driver and accelerator section ($\gamma_D = \gamma_A = 1.67$), and air is used in the intermediate section ($\gamma_I = 1.4$).

The steady states calculated from the P-U diagrams (previously described) are compared to the numerical results (Table 2). We see a good agreement between the numerical results and the analytical solution.

Another way to visualize the results is to produce a numerical x-t diagram, using a numerical schlieren type method. The density field is sampled at discrete times, and then the density gradient is calculated using a standard centered second-order finite-difference method. In order to visualize the gradients better, the function $-log(|\frac{\partial \rho}{\partial x}|)$ is plotted. Figure 6 shows an example of a numerical x-t diagram. The same flow phenomena described in Figure 1 are clearly seen in Figure 6.

It necessary to define a "numerical" test time in order to confirm that the simulation results quantitatively match the analytical results, as Figure 6 only allows for a qualitative comparison. For this study, an average density is calculated in the constant region, and then the numerical test time is defined to be where the density is within 1% of this average value. Figure 5 shows a comparison between the analytical test time and the numerical test time, calculated at the location given by Figure 3. It is understood that fluctuations during the test time in a real experimental facility will be much larger than 1%, but a precise definition of the test time is needed in order to be consitent when trying to find the optimal dimensions for the facility.

The analytical test time is calculated to be 106 μs, and the numerical test time is measured to be 104 μs. Figure 5 also shows that the test times are also slightly offset from each other. This discrepancy is due to the

Table 2. Comparison between numerical results and analytical calculations for the various steady state regions. The numerical values have been averaged over the respective specific section, at $t = 450\mu$s for states $\boxed{2}$ and $\boxed{3}$ and at $t = 600\mu$s for states $\boxed{12}$ and $\boxed{13}$. P, U and ρ are the pressure, velocity and density, respectively.

State Number	Quantity	Numerical Value	Analytical Value
$\boxed{2}$ $\boxed{3}$	P (Pa)	2.65×10^5	2.65×10^5
$\boxed{2}$ $\boxed{3}$	U (m/s)	1.52×10^3	1.52×10^3
$\boxed{2}$	ρ (kg/m^3)	0.461	0.462
$\boxed{3}$	ρ (kg/m^3)	1.67	1.68
$\boxed{12}$ $\boxed{13}$	P (Pa)	9.24×10^4	9.24×10^4
$\boxed{12}$ $\boxed{13}$	U (m/s)	2.14×10^3	2.14×10^3
$\boxed{13}$	ρ (kg/m^3)	0.217	0.218
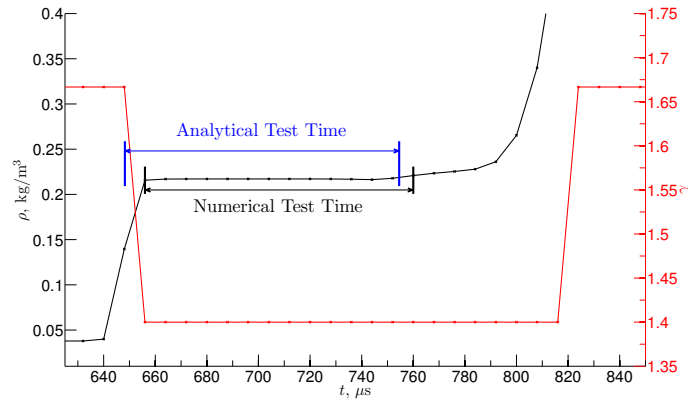
Figure 5. Comparison between the analytical test time and the numerical test time for the 1D case.

numerical methods used. Contact discontinuities, which are infinitely thin in the ideal case, are spread out over many cells in simulations due to numerical diffusion. In addition, the reflection of waves off of a contact discontinuity of finite thickness also introduces errors in the simulations. This explains the small differences between the analytical and numerical test times, though the discrepenancies are minor, and acceptable for this investigation.
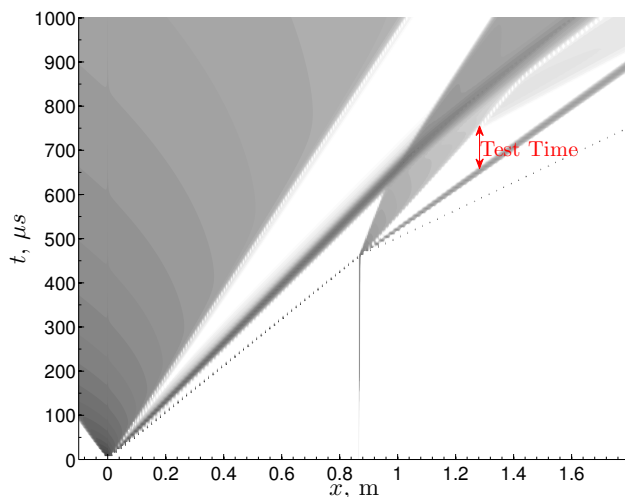

Figure 6. Numerical x-t diagram for a 1D expansion tube with no nozzle. The contours correspond to density gradients in the flow. All of the physical phenomena expected are clearly seen in the flow. The test time is limited by the reflection of the head of the secondary expansion wave reflecting off of the primary contact discontinuity intersection with the tail of the expansion.

VI.B. Quasi-1D Results

The addition of a nozzle to the accelerator tube expands the design parameter space that one must investigate. It is now possible to change the location of the nozzle, the geometry of the nozzle, the nozzle diaphragm burst pressure, and the pressure and type of gas in the nozzle at the beginning of a run. The fill pressures previously specified will be used, and a $10°$ conical nozzle of length $L_N = 0.40$ m is used. This corresponds to an expansion ratio of 10, and was found to generate useful test conditions. The dimensions of the intermediate and accelerator tubes need to be changed from the 1D optimal dimensions in order to maximize the test time once a nozzle has been added.

The nozzle is initially placed at low pressure ($P_N = 100$ Pa), and a burst pressure is specified for the diaphragm that initially separates the accelerator and nozzle sections. A relatively light diaphragm is being used that bursts when the pressure difference between the upstream cell and downstream cell exceeds 30 kPa. Until the diaphragm breaks, it acts as a perfectly reflecting, infinitely stiff wall.

VI.C. Optimization of Test Time with a Nozzle

Figure 7 shows a numerical x-t diagram for the conditions specified in Section VI.A. The interfaces between the driver and the intermediate sections, intermediate and accelerator sections, and accelerator and nozzle sections are located at 0 m, 1.02 m, and 1.27 m respectively. A complex flow phenomenom is created when the helium from the accelerator section enters the diverging nozzle. It is possible to observe an primary shock, contact discontinuity, and secondary shock, which are the same features seen in previous studies on nozzle start up phenomenon.[33]

Unlike in a reflected shock tube, the startup time associated with the nozzle for a VET does not reduce the usable test time. Instead, an unsteady expansion is created when the contact discontinuity between the intermediate and accelerator gases enters the nozzle. The mismatch in sound speeds between these two gases necessitates the creation of an unsteady expansion. It is the trailing characteristic from this unsteady expansion that corresponds to the beginning of the test time. The test time is ended when either the tail of expansion wave from the intermediate/accelerator interface reaches the test location, or when the reflected head of the intermediate/accelerator expansion reaches the test location, which is the same as the 1D case.
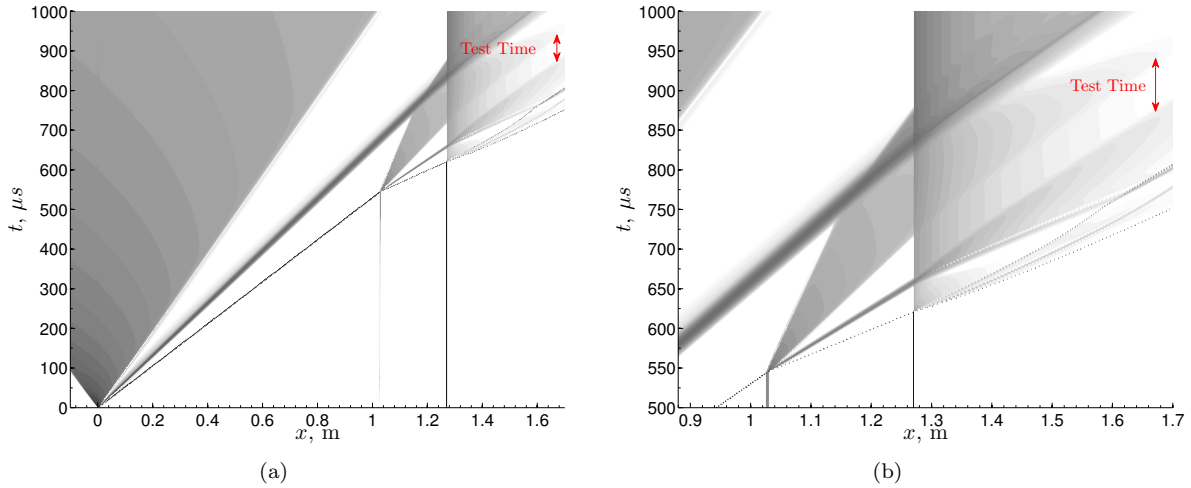
American Institute of Aeronautics and Astronautics

Figure 7. Numerical x-t diagrams for an expansion tunnel with a $10°$ half angle diverging conical nozzle. The entire facility (left (a)) and a close-up of the accelerator section and nozzle (right (b)) are shown.

Figure 8 shows how the predicted test time changes as the lengths of the different sections of the expansion tunnel are changed. For all cases, the sum of the lengths of the intermediate and accelerator sections is limited to 1.27 m. $L_{i,nozzle}$ refers to the length of the intermediate section when a nozzle is also used, and this length is normalized by $L_{i,1D}$, the ideal intermediate section length when no nozzle is used ($L_{i,1D} = 0.86$ m). It is clear that increasing the length of intermediate section (with respect to the 1D case), and therefore reducing the length of the accelerator section, increases the test time. This is because the reflected expansion head wave also travels through the nozzle, so if the accelerator length is not reduced from the 1D case, the reflected head of the expansion wave will end the test time very quickly. All points to the left of the maximum test time are limited by the reflection of the expansion head, and all points to the right of the maximum test time are limited by the expansion tail. The maximum point is approximately where both the reflection of the expansion head and the expansion tail arrive at the test location at the same time. A maximum test time of 66 μs is found when $L_I = 1.02$ m and $L_A = 0.25$ m.
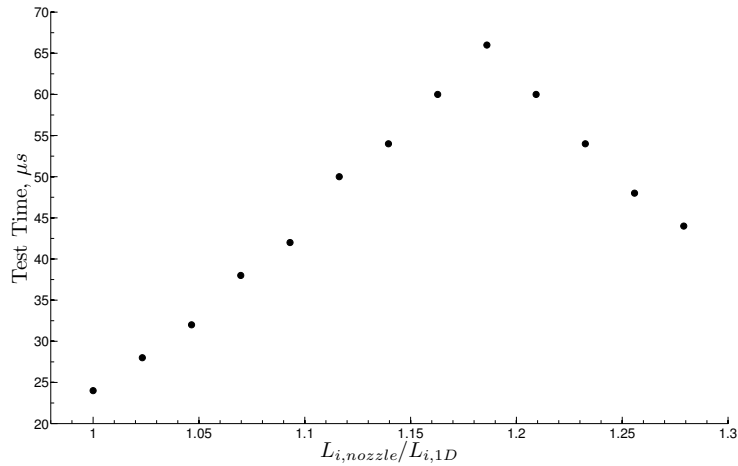

Figure 8. Test time for varying lengths of the intermediate and accelerator sections when using a nozzle. $L_{i,nozzle}$ corresponds to the length of the intermediate section when using a nozzle, and $L_{i,1D}$ corresponds to the ideal intermediate section length in the 1D configuration.

American Institute of Aeronautics and Astronautics

VI.D.   Ideal Fill Conditions

Figure 9 shows plots of γ, ρ, P, u, and M during the chosen test time, where the dimensions have been chosen to maximize the test time. The average flow values are calculated during this test time at a downstream location of $x = 1.67$ m which corresponds to an expansion ratio of 10. During the test time, $\rho = 0.0181$ kg/m^3, $U = 2.54$ km/s, $P = 2.86$ kPa, and $M = 5.40$. This corresponds to a reservoir enthalpy of 3.77 MJ/kg. These values agree very well with the test time conditions predicted by an isentropic steady expansion, which correspond to $\rho = 0.0184$ kg/m^3, $U = 2.54$ km/s, $P = 2.90$ kPa, and $M = 5.41$. Uncertainties are not included on these numerical predictions because non-ideal effects will cause fluctuations during the test time which are not accounted for in the numerical simulations.

Assuming Sutherland's Law for viscosity, these test conditions also correspond to a unit Reynold's number of approximately 1.3×10^6/m.
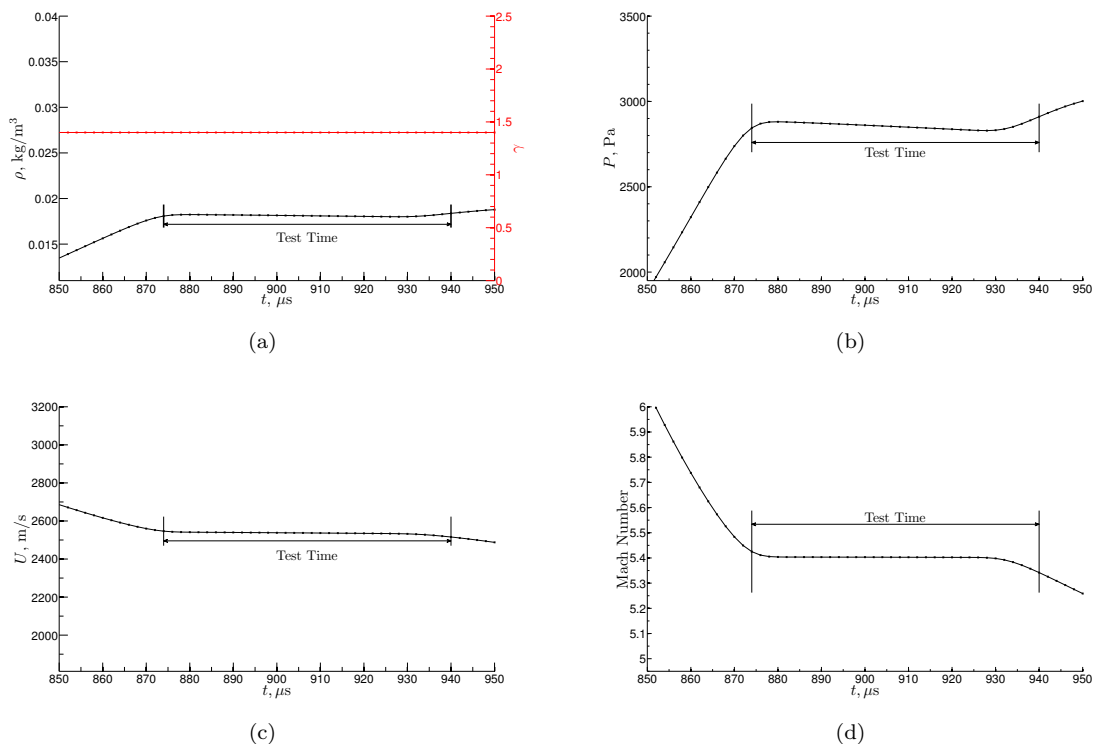

Figure 9. Flow conditions at a point ($x = 1.67$ m) corresponding to an expansion ratio of 10.

In order to show that it is possible to have more than one run condition for a given experimental set-up, simulations were also performed with fill pressures in the intermediate and accelerator tubes doubled and halved from the previously proposed values. The data is still sampled at a downstream location corresponding to an expansion ratio of 10. A summary of these three possible run conditions are summarized in Table 3. It is important to note that the maximum static temperature reached in the half pressure trial is approximately 2350 K, which means that the perfect gas assumption will start to break down. The properties calculated are presented as an estimate since the simulations were run assuming a perfect gas.

American Institute of Aeronautics and Astronautics

Table 3. Comparison between test conditions predicted for varying fill pressures. The double pressure and half pressure cases refer to doubling and halving the fill pressure of both the intermediate and accelerator tubes in comparison to the design conditions. ρ_∞, P_∞, U_∞, and M_∞ are the free-stream density, pressure, velocity and Mach number, respectively. h_R is the effective reservoir enthalpy.

Property	Design Conditions	Double Pressure	Half Pressure
ρ_∞ (kg/m^3)	0.0181	0.0355	0.00925
P_∞ (kPa)	2.86	4.73	1.70
U_∞ (km/s)	2.54	2.29	2.76
M_∞	5.40	5.31	5.44
h_R (MJ/kg)	3.77	3.09	4.45
Test Time (μs)	66	78	38

VII.   Conclusion

The vertical expansion tunnel (VET) has many advantages over the reflected shock tunnel (RST). Three of which are that: the VET does not suffer from driver gas contamination issues; it does not need to heat the test gas to as high a temperature to achieve the same run condition; and it has a wider range of effective reservoir conditions. A disadvantage of a VET relative to a RST is the shorter useful test time. The VET has one primary advantage over a conventional expansion tube (ET), which is that the secondary diaphragm is unnecessary. Without a secondary diaphragm in a VET, the test time is improved and the contamination of the flow by the diaphragm particulates is eliminated. A disadvantage of a VET relative to an ET is the more limited operating parameter space. Perfect-gas quasi-1D gas dynamic computations show the test time of a VET (cold driver, a 0.0254 m diameter tube, and a 10° nozzle) is on the order of 70 μs, which is comparable to existing ET facilities (given the facility sizing, namely tube diameter). The effective reservoir conditions of the VET lie somewhere between the RST and the ET.

Acknowledgments

References

[1]Paul, A. and Stalker, R. J., "Test Flow Disturbances in an Expansion Tube," *Journal of Fluid Mechanics*, Vol. 245, 1992, pp. 493–521.

[2]Trimpi, R. L., "A Preliminary Theoretical Study of The Expansion Tube, a New Device for Producing High-Enthalpy Short-Duration Hypersonic Gas Flows," Nasa tr r-133, 1962.

[3]Trimpi, R. L. and Callis, L. B., "A Pefect-Gas Analysis of the Expansion Tunnel, a Modification to the Expansion Tube," Nasa tr r-223, 1965.

[4]Norfleet, G. D., Lacey, J. J., and Whitfield, J. D., "Results of an Experimental Investigation of the Performance of an Expansion Tube," *Proceedings of the Fourth Hypervelocity Tech. Symp.*, Tullahoma, Tennessee, 1965.

[5]Spurk, J. H., "Design, Operation and Preliminary Results of the BRL Expansion Tube," *Proceedings of the Fourth Hypervelocity Tech. Symp.*, Tullahoma, Tennessee, 1965.

[6]Miller, C. G., "Operational Experience in the Langley Expansion Tube with Various Gases," Nasa tm 78637, 1977.

[7]Neely, A. J. and Morgan, R. G., "The Superorbital Expansion Tube Concept, Experiment and Analysis," *The Aeronautical Journal*, Vol. 98, No. 973, 1994, pp. 97–105.

[8]Erdos, J. I., Bakos, R. J., Castrogiovanni, A., and Rodgers, R. C., "Dual Mode Shock-Expansion/Reflected-Shock Tunnel," *Proceedings of the Thirty Fifth Aerospace Sciences Meeting and Exhibit*, AIAA, Reno, Nevada, 1997.

[9]Sasoh, A., Ohnishi, Y., Ramjaun, D., Takayama, K., Otsu, H., and Abe, T., "Effective Test Time Evaluation in High-Enthalpy Expansion Tube," *AIAA*, Vol. 39, No. 11, 2001, pp. 21412147.

[10]Ben-Yakar, A. and Hanson, R. K., "Characterization of Expansion Tube Flows for Hypervelocity Combustion Studies," *Journal of Propulsion and Power*, Vol. 18, No. 4, 2002, pp. 943–952.

[11]Heltsley, W. N., Snyder, J. A., Houle, A. J., Davidson, D. F., Mungal, M. G., and Hanson, R. K., "Design and Characterization of the Stanford 6 Inch Expansion Tube," *42nd AIAA/ASME/SAE/ASEE Joint Propulsion Conference and Exhibit*, AIAA, 2006.

[12]Dufrene, A., Sharma, M., and Austin, J. M., "Design and Characterization of a Hypervelocity Expansion Tube Facility," *Journal of Spacecraft and Rockets*, Vol. 23, No. 6, 2007, pp. 1185–1193.

[13]Liepmann, H. W. and Roshko, A., *Elements of Gasdynamics*, Dover Publications, 1993.

[14]Goodwin, D. G., "An Open-Source, Extensible Software Suite for CVD Process Simulation," *Electrochemical Society*, 2003, pp. 155–162.

[15]Browne, S., Zeigler, J., and Shepherd, J. E., "Numerical Solution Methods for Shock and Detonation Jump Conditions," GALCIT - FM2006-006, 2006.

[16]Gordon, S. and McBride, B., "Thermodynamic Data to 20 000 K for Monatomic Gases," NASA TP-1999-208523, 1999.

[17]McBride, B., Zehe, M. J., and Gordon, S., "NASA Glenn Coefficients for Calculating Thermodynamic Properties of Individual Species," NASA TP-2002-211556, 2002.

[18]Gupta, R. N., Yos, J. M., Thompson, R. A., and Lee, K. P., "A Review of Reaction Rates and Thermodynamic and Transport Properties for an 11-Species Air Model for Chemical and Thermal Nonequilibrium Calculations to 30000 K," NASA-RP-1232, 1990.

[19]Kao, S. and Shepherd, J. E., "Numerical Solution Methods for Control Volume Explosions and ZND Detonation Structure," FM2006-007, 2006.

[20]Hirschfelder, J. O., Curtiss, C. F., and Bird, R. B., *Molecular Theory of Gases and Liquids*, John Wile and Sons, 1954.

[21]Stalker, R. J. and Mudford, N. R., "Unsteady Shock Propagation in a Steady Flow Nozzle Expansion," *Journal of Fluid Mechanics*, Vol. 241, 1992, pp. 525–548.

[22]Mirels, H., "Shock Tube Test Time Limitation Due to Turbulent-Wall Boundary Layer," *AIAA*, Vol. 2, No. 1, 1963, pp. 84–93.

[23]Mirels, H., "Shock Tube Test Time Limitation Due to Turbulent Wall Boundary Layer," Technical report, Aerodynamics and Propulsion Research Laboratory, Aerospace Corporation, Inglewood, CA, May 1963.

[24]Wintenberger, E., Austin, J. M., Cooper, M., Jackson, S., and Shepherd, J. E., "Analytical Model for the Impulse of Single-Cycle Pulse Detonation Tube," *Journal of Propulsion and Power*, Vol. 19, No. 1, 2003, pp. 22–38.

[25]Glaister, P., "Flux Difference Splitting for the Euler Equations in One Spatial Co-ordinate with Area Variation," *International Journal for Numerical Methods in Fluids*, Vol. 8, 1988, pp. 97–119.

[26]Roe, P. L., "Approximate Riemann Solvers, Parameter Vectors, and Difference Schemes," *Journal of Computational Physics*, Vol. 43, No. 2, 1981, pp. 357–372.

[27]Abgrall, R. and Karni, S., "Computations of Compressible Multifluids," *Journal of Computational Physics*, Vol. 169, No. 2, 2001, pp. 594–623.

[28]Purser, R. J. and Leslie, L. M., "An efficient interpolation procedure for high-order three-dimensional semi-Lagrangian models," *Monthly weather review*, Vol. 119, No. 10, 1991, pp. 2492–2498.

[29]Leveque, R. J., *Finite Volume Methods for Hyperbolic Problems*, Cambridge Texts in Applied Mathematics, 2007.

[30]Leer, B. V., "Towards the Ultimate Conservative Difference Scheme II. Monotonicity and conservation combined in a second order scheme," *Journal of Computational Physics*, Vol. 14, No. 4, 1974, pp. 361–370.

[31]Lax, P. D. and Liu, X.-D., "Solution of Two-Dimensional Riemann Problems of Gas Dynamics by Positive Schemes," *SIAM Journal on Scientific Computings*, Vol. 2, No. 2, 1998, pp. 319–340.

[32]Sanders, R., Morano, E., and Druget, M.-C., "Multidemsional Dissipation for Upwind Schemes: Stability and Applications to Gas Dynamics," *Journal of Computational Physics*, Vol. 145, 1998, pp. 511–537.

[33]Smith, C. E., "The starting process in a hypersonic nozzle," *Journal of Fluid Mechanics*, Vol. 24, 1966, pp. 625–640.